Research article

In silico mechanics and TGF-ß expression of stem cells intramyocardially transplanted with a biomaterial injectate for treatment of myocardial infarction

YD Motchon[1]*, KL Sack[1,2], MS Sirry[1,3], NJ Nchejane[1], T Abdalrahman[1], J Nagawa[1], M Kruger[4], E Pauwels[5,6], D Van Loo[5,7], A De Muynck[5], L Van Hoorebeke[5], NH Davies[4], T Franz[1,8]*

[1]Biomedical Engineering Research Centre, Division of Biomedical Engineering, Department of Human Biology, University of Cape Town, Observatory, South Africa

[2]Cardiac Rhythm Management, Medtronic Inc, Minnesota, USA

[3]Department of Biomedical Engineering, School of Engineering and Computing, American International University, Al Jahra, Kuwait

[4]Cardiovascular Research Unit, MRC IUCHRU, University of Cape Town, Observatory, South Africa

[5]Centre for X-ray Tomography, Department of Physics and Astronomy, Ghent University, Ghent, Belgium

[6]Current affiliation: Nuclear Medicine, University Hospitals Leuven, Leuven, Belgium

[7]Current affiliation: XRE nv, Bollebergen 2B box 1, 9052 Ghent, Belgium

[8]Bioengineering Science Research Group, Department of Mechanical Engineering, Faculty of Engineering and Physical Sciences, University of Southampton, Southampton, United Kingdom

*Corresponding authors: Dodzi.Motchon@uct.ac.za, Thomas.Franz@uct.ac.za

ORCIDs:

YD Motchon: 0000-0002-6222-3483 KL Sack: 0000-0002-8253-1504 MS Sirry: 0000-0003-3735-0963 NJ Nchejane: 0000-0003-3983-7476 T Abdalrahman: 0000-0002-0320-811X J Nagawa: 0000-0002-3712-9647 M Kruger:	E Pauwels: 0000-0002-3296-8011 D Van Loo: A De Muynck: L Van Hoorebeke: NH Davies: 0000-0003-0432-4515 T Franz: 0000-0002-1504-3842

Abstract

Biomaterial and stem cell delivery are promising approaches to treating myocardial infarction. However, the mechanical and biochemical mechanisms underlying the observed therapeutic benefits require further clarification. This computational study aimed to assess deformation and resulting transforming growth factor β (TGF-β) expression of stem cells injected with the biomaterial into the infarcted heart. A microstructural finite element model of a mid-wall equatorial infarcted myocardial region was developed from *ex vivo* microcomputed tomography data of a rat heart with left ventricular infarct and intramyocardial biomaterial injectate. Nine cells were numerically seeded in the injectate of the microstructural model. The microstructural and a previously developed biventricular finite element model of the same rat heart were used to quantify the deformation of the cells during a cardiac cycle for a biomaterial elastic modulus (E_{inj}) ranging between 4.1 and 405,900 kPa. The cellular TGF-β expression was determined with a mathematical relationship of deformation and TGF-β expression developed from existing experimental data and single-cell finite element analysis. Deformation and TGF-β expression of the transplanted cells were largest at E_{inj} of 7.4 kPa, matching that of the cells, and decreased for an increase and decrease in E_{inj}. Cell deformation and TGF-β expression were more sensitive to E_{inj} changes for softer ($E_{inj} \leq 738$ kPa) than stiffer biomaterials. Combining the microstructural and biventricular finite element models enables quantifying micromechanics and signalling of transplanted cells in the heart. The platform offers broader scope for *in silico* investigations of biomaterial and cell therapies for myocardial infarction and other cardiac pathologies.

Keywords: Biomaterial injection therapy; Cell mechanics; Cellular signalling; Cell therapy; Finite element method; Mechanotransduction

Symbols

Symbol	Description
$\bar{a}$	Material parameter, dimension of stress
$\bar{a}_{fs}$	Material parameter defining coupling from in the fibre and sheet directions, with a dimension of stress
$\bar{a}_i$	Material parameter, defined for i = f and s in the fibre and sheet directions, respectively, with stress dimension
B	Governs the shape of peak isometric tension-sarcomere length relation
b	Dimensionless material parameter in Holzapfel model
b_{fs}	Material parameter defining coupling from in the fibre and sheet directions, dimensionless
b_i	Material parameter, defined for i = f and s in the fibre and sheet directions, respectively, dimensionless
C_{10}	Coefficient used in Abaqus to describe the material stiffness in a Neo-Hookean strain energy density function
Ca_0	Peak intracellular calcium concentration
D	Myocardium material's incompressible parameter
D_1	Injectate or cellular material's incompressible parameter
E	Elastic modulus
ECa_{50}	Length-dependent calcium sensitivity
F	Deformation gradient tensor
h	Parameter to define the pathological degree of the tissue
I_{4f}	Transversely isotropic invariant in the fibre direction
I_{4s}	Transversely isotropic invariant in the sheet direction
I_{8fs}	Orthotropic invariant from coupling in fibre and sheet direction
I_i	Isotropic invariants in principal directions

J	Measures the volume change of compressible materials
l	Sarcomere length (time-varying model in active contraction)
l_r	Initial sarcomere length (time-varying model in active contraction)
p	Parameter scaling the isotropic response of the diseased tissue
$\mathbf{T}$	Stress tensor
$\mathbf{T_a}$	Active stress tensor
T_{max}	Constitutive law scaling factor (time-varying model in active contraction)
$\mathbf{T_p}$	Passive stress tensor
t	Time
t_r	Linear function of sarcomere length
t_0	Time to reach peak tension (time-varying model in active contraction)
W	Strain energy density function
ε_{Cell}	Cell strain
ε_{Sub}	Substrate strain
κ	Bulk modulus
λ	Stretch
ν	Poisson's ratio
ω	Variable in the internal variable function depending on time and sarcomere length
σ	Stress

1. Introduction

Cardiovascular disease related deaths are predicted to rise from 17.5 million (i.e. 31% of global deaths) in 2012 to 22.2 million by 2030 (Mendis et al. 2011; Di Angelantonio et al. 2019). In low- and middle-income countries, such as South Africa, the number of affected people in the working-age population is increasing (Finegold et al. 2013; Opie and Mayosi 2005).

Myocardial infarction (MI) causes cardiac cell death in the affected myocardial region, leading to scar formation, ventricular remodelling, and heart failure in the long term.

Transplanting stem cells into the myocardium with injectable biomaterials has gained substantial interest in MI therapy research. The delivered stem cells are expected to promote regenerative reactions in the impaired tissue (Ciuffreda et al. 2018) and can differentiate into cardiac-like cells and endothelial cells (EC) necessary for revascularisation and functional recovery of the heart (Ye et al. 2013; Alrefai et al. 2015).

Pre-clinical studies have demonstrated the beneficial effects of adult stem cell transplantation on MI. For example, Tomita et al. (1999) demonstrated that intramyocardial transplantation of bone marrow-derived stem cells in the rat model improved angiogenesis and cardiac function and reported differentiation into cardiac-like cells (*in vitro* and *in vivo*) in the infarcted myocardium. Wang et al. (2018) reported an increase in the expression of endothelial-related proteins, improved ejection fraction, reduced infarct size and a high vessel density by using a biochemically and genetically activated hydrogel loaded with adipose-derived stem cells in rats.

Clinical studies also reported the benefits of cell transplantation in MI. These benefits include the differentiation into cardiac-like cells (Beltrami et al. 2003; Guo et al. 2011; Robinton and Daley 2012) and enhanced neovascularisation and angiogenesis with reduced cardiomyocyte death through paracrine or autocrine signalling (Kocher et al. 2001; Shudo et al. 2013). Strauer and Steinhoff (2011) observed improvement in cardiac function in patients with MI six months after human mesenchymal stem cell (MSC) transplantation.

Pre-clinical and clinical studies support the hypothesis that paracrine signalling drives the beneficial effects of cell transplants in MI (Duran et al. 2013; Nguyen et al. 2016; Wang et al. 2018; Strauer and Steinhoff 2011; Gao et al. 2015; Tomita et al. 1999; Kocher et al. 2001; Shudo et al. 2013; Gnecchi et al. 2008). During cellular communication in cell-based therapies, proteins such as growth factors are released by a cell and attached to membrane receptors of

the same or another cell through autocrine and paracrine effects. These processes are essential in the mechanotransduction of the injected cells in the dynamic mechanical environment of the heart.

Mechanical stimuli, through mechanotransduction, are essential for growth factors production and proteins responsible for angiogenic phenotypes in the heart (Bhang et al. 2010; Tian et al. 2016). Zheng et al. (2001) reported an increase in vascular endothelial growth factor (VEGF) mRNA and its associated protein concentration in cardiac cells exposed to cyclic stretching and a 2.5-fold increase in transforming growth factor-beta (TGF-β) one hour post-stretching. More importantly, they observed that neutralising TGF-β inhibited the stretch-induced production of VEGF, confirming the mediation role of TGF-β in VEGF production. The link between the mechanically stimulated growth factor secretion and beneficial effects on the infarcted heart was also demonstrated *in vivo* by several pre-clinical studies (Cassino et al. 2012; Zhao et al. 2016; Rashid et al. 2021).

The physical environment of cells transplanted in the infarcted heart is essential in cell therapies. A biomaterial as a carrier and scaffold for the transplanted cells constitutes the immediate microenvironment which transmits mechanical stimuli from the myocardium to the cells. The biomaterial contributes to the mechanics of the surrounding infarcted myocardium and the embedded cells. Hence, the biomaterial offers a vehicle for improving wall mechanics and ventricular function and enhancing paracrine cardioprotective signalling through cellular mechanotransduction.

Therefore, this study aimed to develop computational models to predict the mechanics and associated signalling of cells transplanted in a carrier biomaterial intramyocardially in an infarcted heart and demonstrate the ability of the developed models to optimise cell therapies for myocardial infarction. A multi-scale finite element approach was used to represent an *in situ* biomaterial injectate in a rat heart with an LV infarct and determine the quantitative relationship between TGF-β production of stem cells embedded in the biomaterial and the biomaterial's stiffness.

2. Materials and methods

2.1 Geometrical modelling

2.1.1 Biventricular geometry of an infarcted rat heart with biomaterial injectate

A three-dimensional biventricular (BV) geometry of a rat heart with LV infarct and polymeric injectate developed previously from *ex vivo* microcomputed tomography (µCT) image data (Motchon et al. 2023) was used in the current study. In brief, a male Wistar rat (body mass: 180-220 g) received a myocardial infarction by permanent ligation of the left anterior descending coronary artery and, seven days later, an injection of 100 µl of radiopaque silicone rubber containing lead chromate (Microfil® MV-120 Flow-Tech, Carver, MA, USA) into the infarcted LV region. Following dispersion and *in situ* polymerisation of the Microfil® material, the animal was humanely killed, and the heart was carefully harvested, fixed in a 4% paraformaldehyde solution, and transferred to saline. The heart underwent microcomputed tomography (µCT) scanning with 1801 projections and an exposure time of 0.8 s, providing images with a voxel pitch of 10 µm (custom-made scanner with Feinfocus X-ray tube and Varian 2520V Paxscan a-Si flat panel detector, Centre for X-ray Tomography, Ghent University, Belgium (Masschaele et al. 2007)).

The procedure to develop the biventricular geometry followed the same procedure described by Motchon et al. (2023). In brief, the biventricular geometry was reconstructed from the µCT image stack by a semi-automated segmentation (region-growing, level-set thresholding, and manual selection) using two masks to represent the myocardium and the polymeric injectate (Simpleware ScanIP, Synopsys). The resulting geometry captured the essential morphology of the left and right ventricle and microstructural details of the dispersed intramyocardial injectate in the LV free wall (Figure 1a). The geometry was meshed with 147,240 and 58,902 quadratic tetrahedral elements in the myocardial and injectate region, respectively (Simpleware ScanIP). The mesh density varied between 302.8 mm^{-3} in the myocardium and 3,852.3 mm^{-3} in the injectate (Figure 1b). The volumetric tetrahedral meshed geometry was imported in Abaqus 6.14-3 CAE (Dassault Systèmes, Providence, RI, USA) and the infarct region was approximated in the antero-apical LV region (Figure 1c).

A rule-based approach was used to define myocardial fibre orientation from -50° at the epicardial to 80° at the endocardial surface, as described previously (Motchon et al. 2023). The fibre orientation data were incorporated into the biventricular FE model in Abaqus.

2.1.2 Microstructural LV mid-wall geometry and transplanted cells

To better represent the microstructural details of the dispersed polymer injectate in the infarcted myocardium, an LV mid-wall volume of 748 µm x 748 µm x 722 µm in the infarct region was extracted by resampling the entire heart geometry (Simpleware ScanIP) (Figure 1d). The spacing in the x, y, and z directions was decreased from 30 µm in the BV geometry to 7.8 µm to accommodate the small dimensions of the transplanted cells in the injectate region.

Nine cells transplanted within the intramyocardial injectate were incorporated by numerical seeding using an idealised spherical shape, distinguishing membrane, cytoplasm and nucleus. A Python script was created and implemented in Simpleware ScanIP to seed multiple cells randomly in the sub-model's injectate region. For one cell, the process comprised creating three concentric spherical surfaces with diameters of 60, 55, and 20 µm for the membrane, cytoplasm, and nucleus (Figure 1d). A Boolean subtraction allowed obtaining a thickness of 5 µm and 35 µm for the membrane and the cytoplasm, respectively. Finally, the tree component-assembly was placed in the injectate at a randomly chosen location.

Discretised domains were defined in Abaqus for finite element analysis from the resulting meshed sub-model geometry. The mesh comprised 320,653 10-node tetrahedral elements (C3D10M), i.e. 2,552, 168,746 and 149,355 elements for the myocardium, injectate and the nine cells, respectively. The mesh size of the cellular components varied amongst the nine cells based on the meshing process and was 6,101 ± 42 in the cell membrane, 8,710 ± 299 in the cytoplasm and 1,784 ± 82 in the nucleus.

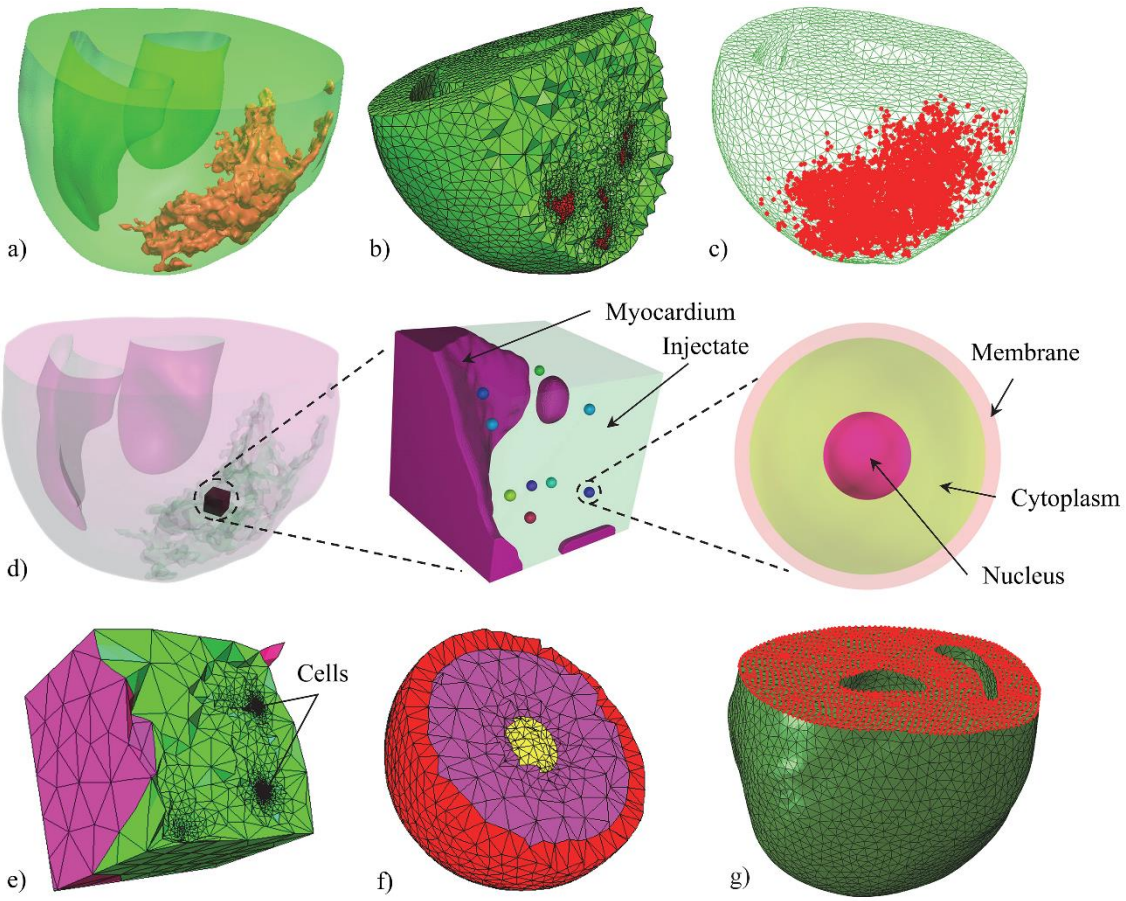

Figure 1. Geometries and models developed from the biventricular rat geometry to the microstructure extracted from the left ventricle mid-wall with transplanted cells in the injectate region. a) Biventricular geometry showing myocardium (green translucent) and injectate (beige). b) Meshed biventricular geometry with a cross-section illustrating the difference in mesh density between myocardium (green) and injectate (red). c) Meshed biventricular geometry illustrating the infarct region (red). d) Development of a microstructural left ventricle mid-wall geometry (sub-model). Left: Biventricular geometry showing the size and location of the sub-model region. Middle: Sub-model geometry comprising myocardium, injectate and nine transplanted cells. e) Meshed sub-model geometry with coarse mesh for the myocardium and injectate and fine mesh for the cells. f) Cross-sectional view of meshed geometry of single cell showing membrane (red), cytoplasm (pink) and nucleus (yellow). g) The biventricular FE mesh's basal nodes (red) were fixed as the boundary condition for simulations.

2.2 Constitutive laws

2.2.1 Healthy and infarcted myocardium

The passive mechanical behaviour of the myocardium was represented by a hyperelastic anisotropic law using a modified strain energy density function from Holzapfel and Ogden (2009). Changes were introduced to describe the pathological stage of the myocardium (Sack et al. 2018). The passive mechanical response of infarcted myocardium depends on the stage of the infarct (Holmes et al. 2005; Holmes et al. 1997; Tyberg et al. 1974; Villarreal et al. 1991). Here, a one-week infarct was modelled. The associated increased stiffness in the fibre, circumferential, and longitudinal directions (Hood et al. 1970) was implemented using parameters h and p in Eqn. (2), where h = 1 and 0 represent healthy and infarcted myocardium, respectively (Sack et al. 2018).

$$W = \frac{\bar{a}}{2b} e^{b(I_1-3)} + \sum_{i=f,s} \frac{\bar{a}_i}{2b_i}\left\{e^{b_i(I_{4i}-1)^2} - 1\right\} + \frac{\bar{a}_{fs}}{2b_{fs}}\left\{e^{b_{fs}(I_{8fs})^2} - 1\right\} + \frac{1}{D}\left(\frac{J^2-1}{2} - \ln(J)\right) \tag{1}$$

with

$$\begin{aligned} \bar{a} &= a(h + (1-h)p), \\ \bar{a}_i &= a_i(h + (1-h)p) \text{ and} \\ \bar{a}_{fs} &= a_{fs}(h + (1-h)p). \end{aligned} \tag{2}$$

The active contraction of the myocardium was implemented with a time-varying elastance approach with an additional term to consider the passive response during the contraction (Guccione and McCulloch 1993; Guccione et al. 1993; Walker et al. 2005) and a tissue health parameter h to represent the pathological stage of the myocardium (Sack et al. 2018):

$$T_a(t, E_{ff}) = \frac{T_{max}}{2} \frac{Ca_0^2}{Ca_0^2 + EC_{a_{50}}^2(E_{ff})} \left(1 - \cos\left(\omega(t, E_{ff})\right)\right) h \tag{3}$$

with

$$ECa_{50}^2(E_{ff}) = \frac{Ca_{0_{max}}}{\sqrt{e^{B(l(E_{ff})-l_0)} - 1}}, \tag{4}$$

and

$$\omega(t, E_{ff}) = \pi \frac{t}{t_0}, \text{for } 0 \leq t \leq t_0$$

$$\omega(t, E_{ff}) = \pi \frac{t - t_0 + t_r(l_r)}{t_r(l)}, \text{for } t_0 \leq t \leq t_r \tag{5}$$

$$\omega(t, E_{ff}) = 0, \text{for } t \geq t_0 + t_0$$

The additive approach was used to compute the total tension in the myocardium where the time-varying active tension $\mathbf{T_a}$ (Eqn. (3)) was combined with the tension derived from the passive response $\mathbf{T_p}$:

$$\mathbf{T} = \mathbf{T_a} + \mathbf{T_p} \tag{6}$$

The values of the active and passive constitutive parameters used are provided in the Supplemental Tables 1 and 2.

2.2.2 Injectable biomaterial

The injectable biomaterial, e.g. a polyethylene glycol (PEG) hydrogel, was described by a hyperelastic isotropic incompressible Neo-Hookean material model:

$$W = C_{10}(I_1 - 3) \tag{7}$$

where I_1 is the first deviatoric strain invariant, and C_{10} characterises the material stiffness obtained from the elastic modulus E_{inj} and the Poisson's ratio ν_{inj}:

$$C_{10} = \frac{E_{inj}}{4(1 + \nu_{inj})} \tag{8}$$

with ν_{inj} = 0.5 defining incompressibility and E_{inj} varied between 4.1 and 405,900 kPa (see section 2.5 FE simulations and data analysis for more details).

2.2.3 Cells

Cell membrane, cytoplasm and nucleus were treated as hyperelastic isotropic compressible material described with a Neo-Hookean strain energy density function (Caille et al. 2002; Saeed et al. 2016):

$$W = C_{10}(I_1 - 3) + \frac{1}{D_1}\left(J^{el} - 1\right)^2, \tag{9}$$

where J^{el} is a measure of volume change of the compressible material, and C_{10} and D_1 depend on the elastic modulus and the material compressibility, i.e.

$$J^{el} = \det(\mathbf{F}) \tag{10}$$

$$C_{10} = \frac{E}{4(1+\nu)} \tag{11}$$

$$D_1 = \frac{2E}{3(1-2\nu)}. \tag{12}$$

$\bar{I}_1$ is the first deviatoric strain invariant defined in terms of deviatoric or principal stretches ($\bar{\lambda}_i$ with i = 1, 2, 3):

$$I_1 = \lambda_1^2 + \lambda_2^2 + \lambda_3^2 \tag{13}$$

The material parameter values used for the cellular components are given in Supplemental Table 3.

2.3 Boundary conditions and loading

The boundary and loading conditions for the BV model were described in detail previously (Motchon et al. 2023). In brief, zero displacement in the longitudinal direction was applied to the nodes at the basal surface to prevent the rigid body motion of the BV geometry (Figure 1g). The passive filing was implemented with a linearly increasing pressure load on LV and RV cavity surfaces. Several studies reported a higher cavity pressure in the LV than in the RV. In normal human hearts, systolic pressure was 30-40 mmHg in the RV and 100-140 mmHg in the LV (Mininni et al. 1996; Reichek and Devereux 1982). Pacher et al. (2004) reported end-diastolic and end-systolic LV pressure in rats of 3.8 ± 0.9 mmHg and 133.8 ± 8.1 mmHg, respectively. In the current study, the cavity pressure was increased from 0 to 3.0 mmHg for the LV and from 0 to 0.75 mmHg for the RV.

Boundary conditions and loading for the microstructural mid-wall sub-model were obtained from the biventricular model (Motchon et al. 2023) by employing the sub-modelling technique in Abaqus. The nodal displacements of the sub-model mid-wall region in the BV model were recorded for an entire cardiac cycle and applied as boundary conditions and displacement loading to the sub-model surfaces.

2.4 Cell deformation and TGF-β production

The mechanical cues sensed by cells were assumed to originate from the deformation of the intramyocardial injectate during the cardiac cycle. A mathematical model was developed to predict the amount of TGF-β expressed by the transplanted mesenchymal stem cells due to the deformations induced by heart activities. The model related the TGF-β concentration measured experimentally in cells exposed to substrate stretch (Hirakata et al. 1997) to the corresponding cellular strain predicted with a finite element model.

2.4.1 Mechanics of a single cell on an elastic substrate subjected to stretch

A finite element model of a single cell attached to an elastic substrate was developed to simulate the biaxial stretch experiments reported by Hirakata et al. (1997). A spherical cap with a diameter of 20 µm and a central thickness of 2 µm was used to represent the cell. The spherical cap was attached to the centre of a planar substrate (100 µm x 100 µm, thickness 2 µm) using 37 disks representing focal adhesions (FA) (diameter 2 µm, thickness 0.5 µm). These disks were equally distributed over the basal cell surface. Each disk was 2.8 µm from the nearest adjacent disk (Figure 2). The cell-FA and FA-substrate contact were modelled using tie constraints to ensure permanent adhesion and prevent sliding.

The model geometries were meshed (Abaqus 6.14-3, Dassault Systèmes, Providence, RI, USA) with 4,134 10-node tetrahedral elements (C3D10) for the cell, 14,946 6-node linear triangular elements (C3D6) for each FA disk, and 2,809 8-nodes hexahedral elements (C3D8H) for the substrate. The cell and the FA disks were represented as hyperelastic material with a Neo-Hookean strain energy density function, Eqn. (9), and the substrate was described using a linear-elastic model. The parameters used are provided in Supplemental Table 4.

Two substrate edges were fixed, and a displacement was applied to the other two edges to generate an equibiaxial strain of up to 20% (Figure 2d).

The average strain in the cell and the focal adhesions were recorded and related to the applied substrate strain. A linear fit was then used to express the cellular deformation as a function of the substrate strain, see Eqn. (15).

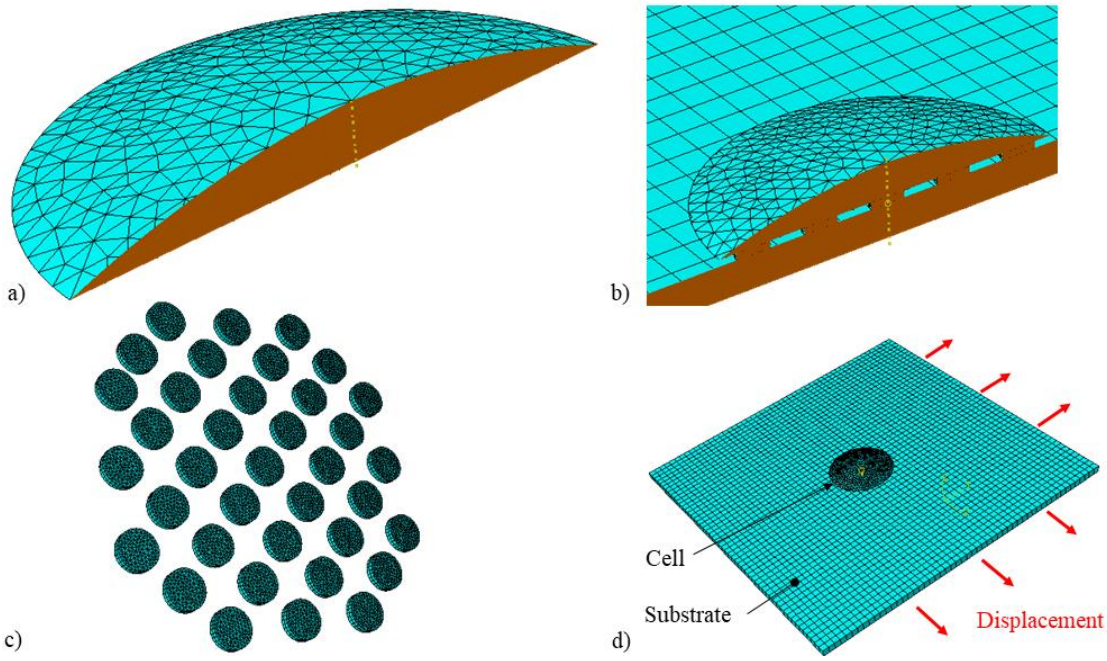

Figure 2. Geometrical details of finite element model for single-cell stretching. a) Spherical cap representing the cell. b) Cross-sectional view of the cell attached to the substrate with focal adhesion disks. c) Arrangement of focal adhesion disks. d) Cell attached to the centre of the substrate with the illustration of displacement of two substrate edges to generate biaxial strain in the substrate.

2.4.2 TGF-β production in cells exposed to substrate stretch

Several experimental studies have quantified the mechanically-induced growth factor release in cells (Cassino et al. 2012; Hirakata et al. 1997; Galie et al. 2012). Hirakata et al. (1997) measured mRNA expression for TGF-β induced by cyclic mechanical stretch. In the study, rat mesangial cells were cultured on an elastic substrate and subjected to a biaxial substrate strain of different amplitudes (5%, 10%, 15% and 20%). The concentration of TGF-β mRNA expression was reported as a function of the substrate strain amplitude (Hirakata et al. 1997, Fig. 3). These data were utilised in the current study to derive a linear function of TGF-β expression with the substrate strain:

$$\text{TGF-}\beta = a_0\, \varepsilon_{Sub} + b_0, \tag{14}$$

where $a_0 = 0.06$, $b_0 = 0.08$, and ε_{Sub} is the substrate strain.

A linear relationship between the average strain in the cell and the substrate strain can be derived from simulations with the FE model described in the previous section:

$$\varepsilon_{Cell} = a_1 \varepsilon_{Sub} + b_1, \tag{15}$$

with a_1 and b_1 calibrated from a linear fit.

Combining Eqns. (14) and (15), the expression of TGF-β mRNA can be represented as a function of cellular strain:

$$\text{TGF-}\beta = a_2 \varepsilon_{cell} + b_2\,, \tag{16}$$

and a_2 and b_2 be determined by eliminating ε_{Sub} in Eqns. (14) and (15).

2.5 FE simulations and data analysis

A parametric study with the variation of the elastic modulus of the biomaterial injectate in the range of E_{inj} = 4.1 to 405,900 kPa (i.e. 4.1, 7.4, 40.6, 73.8, 405.9, 738, 4,059, 7,380, 40,590, 73,800 and 405,900 kPa) was conducted to determine the impact of injectate stiffness on the deformation of the biomaterial injectate and the transplanted cells in the injectate in the left-ventricular mid-wall region.

The deformation of injectate and cells was assessed using minimum and maximum principal strains.

The analysis of cellular deformation comprised the following strain parameters:

i) The element strain, i.e. the mean value of the strain at the integration points of an element:

$$\varepsilon_{El,j} = \frac{1}{P} \sum_{i=1}^{P} \varepsilon_{IP,i}\,, \tag{17}$$

where $\varepsilon_{IP,i}$ is the strain at integration point i, and P is the total number of integration points of element j in the cell mesh.

ii) The volume-averaged strain for a cellular component (i.e. membrane, cytoplasm or nucleus) of cell k:

$$\varepsilon_{CC,k} = \frac{1}{V}\sum_{j=1}^{N} v_j\, \varepsilon_{El,j} \tag{18}$$

where V is the total volume of the region considered, N is the total number of elements in the considered cell component, v_j is the volume of element j, and $\varepsilon_{El,j}$ is the element strain of element j calculated with Eqn. (17)**Error! Reference source not found.**.

iii) The mean strain in a cell component for all cells in the model:

$$\varepsilon_{CC} = \frac{1}{n}\sum_{k=1}^{n} \varepsilon_{CC,k}\,, \tag{19}$$

where $\varepsilon_{CC,k}$ is the volume-averaged in a cell component (membrane, cytoplasm or nucleus) of cell k according to Eqn. (18), and n is the total number of cells in the model (n = 9 in the current study).

iv) The mean strain in the entire cell for all n cells in the model, also referred to as cell strain:

$$\varepsilon_{Cell} = \frac{1}{3}\sum_{l=1}^{3} \varepsilon_{CC} \tag{20}$$

for the three cell components, i.e. membrane, cytoplasm and nucleus, where ε_{CC} is the mean strain in a cell component for all cells in the model according to Eqn. (19).

Descriptive statistical analysis was performed on the strain data in the different model components to determine the normality (Shapiro-Wilk normality test) and variability (SciPy, https://scipy.org/ and NumPy, https://numpy.org/). Data are presented as mean and standard deviation if normally distributed, else as median and interquartile ranges.

3. Results

3.1 Deformation of injectate in the microstructural mid-wall model

At end-diastole, the median maximum principal strain in the injectate decreased from 6.5% to 0.9%, and the median minimum principal strain decreased in magnitude from -7.3% to -0.9% with increasing injectate elastic modulus of E_{inj} = 4.1 to 405,900 kPa (Figure 3 a and b). At end-systole, the median maximum principal strain decreased from 43.8% to 1.4%, and the

median minimum principal strain decreased in magnitude from -38.0% to -1.5% with increasing injectate elastic modulus (Figure 3 c and d). The ratio of end-systolic to end-diastolic maximal principal strain decreased from 6.7 (for the softest injectate with E_{inj} = 4.1 kPa) to 1.6 (for the stiffest injectate with E_{inj} = 405,900 kPa). A similar decrease from 5.2 for the softest injectate to 1.6 for the stiffest injectate was observed for the end-systolic to end-diastolic minimum principal strain ratio.

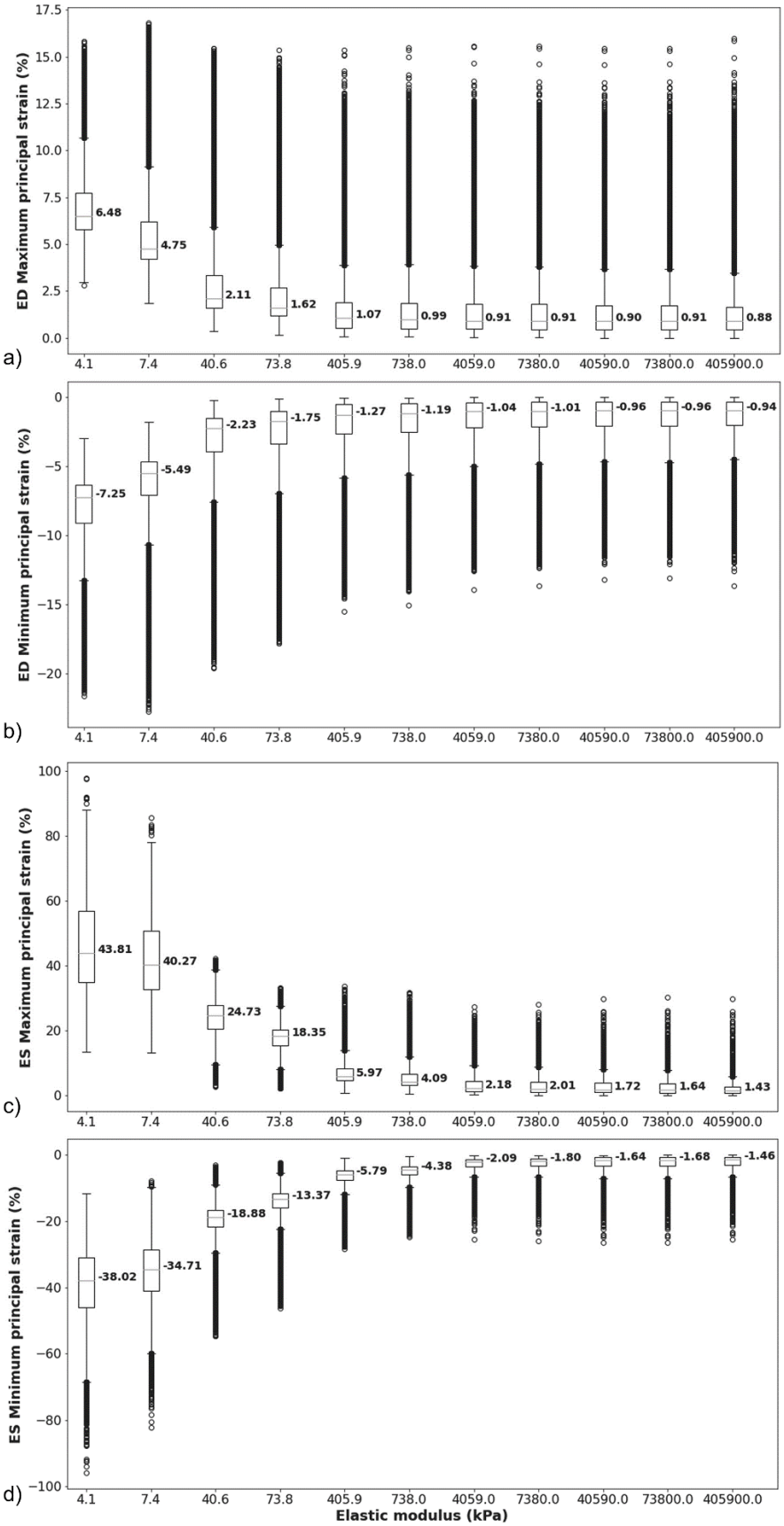
a)
ED Maximum principal strain (%)
6.48
4.75
2.11
1.62
1.07
0.99
0.91
0.91
0.90
0.91
0.88
b)
ED Minimum principal strain (%)
-7.25
-5.49
-2.23
-1.75
-1.27
-1.19
-1.04
-1.01
-0.96
-0.96
-0.94
c)
ES Maximum principal strain (%)
43.81
40.27
24.73
18.35
5.97
4.09
2.18
2.01
1.72
1.64
1.43
d)
ES Minimum principal strain (%)
-38.02
-34.71
-18.88
-13.37
-5.79
-4.38
-2.09
-1.80
-1.64
-1.68
-1.46
4.1
7.4
40.6
73.8
405.9
738.0
4059.0
7380.0
40590.0
73800.0
405900.0
Elastic modulus (kPa)

Figure 3. End-diastolic and end-systolic principal strains in the injectate of the sub-model for different values of the injectate elastic modulus. Maximum (a) and minimum principal strain (b) at end-diastole, and maximum (c) and minimum principal strain (d) at end-systole. (Box and whiskers indicate the median (red line in box), interquartile range (IQR) between first and third quartile (lower and upper box bound), 1.5x IQR (lower and upper whisker), and data points smaller or larger than 1.5x IQR (open circles). Each data point represents the strain value ε_{EL} in an element of the finite element mesh. Data larger or smaller than 1.5x IQR are not considered outliers but actual data.)

3.2 Deformation of transplanted cells in the injectate

The volume-averaged strain is reported for the membrane, cytoplasm, and nucleus of nine cells. The end-systolic and end-diastolic maximum principal strain, Eqn. (20), in the cell components decreased for increasing injectate elastic modulus (Figure 4 a-c). The strain decrease was larger in the lower range of the injectate elastic modulus from E_{inj} = 7.4 kPa to 738 kPa than for higher values of the injectate elastic modulus E_{inj} > 738 kPa. The membrane displayed the highest strain compared to the cytoplasm and nucleus, which exhibited similar strains. Similar results were observed for the minimum principal strain in the cell components, exhibiting negative values indicative of compression (Figure 4 d-f). The strain magnitude decreased for E_{inj} = 7.4 kPa to 738 kPa and levelled off for E_{inj} > 738 kPa.

Increases in maximum and minimum principal strains at the end-systolic time point were observed for an increase of the injectate elastic modulus from E_{inj} = 4.1 kPa to 7.4kPa.

The ES-ED range of the median maximum principal strains decreased for increasing injectate elastic modulus E_{inj} = 7.4 kPa to 405,900 kPa (Figure 4d). The ES-ED median range of maximum and minimum principal strain reflects the deformation range to which the embedded cells are exposed during a cardiac cycle.

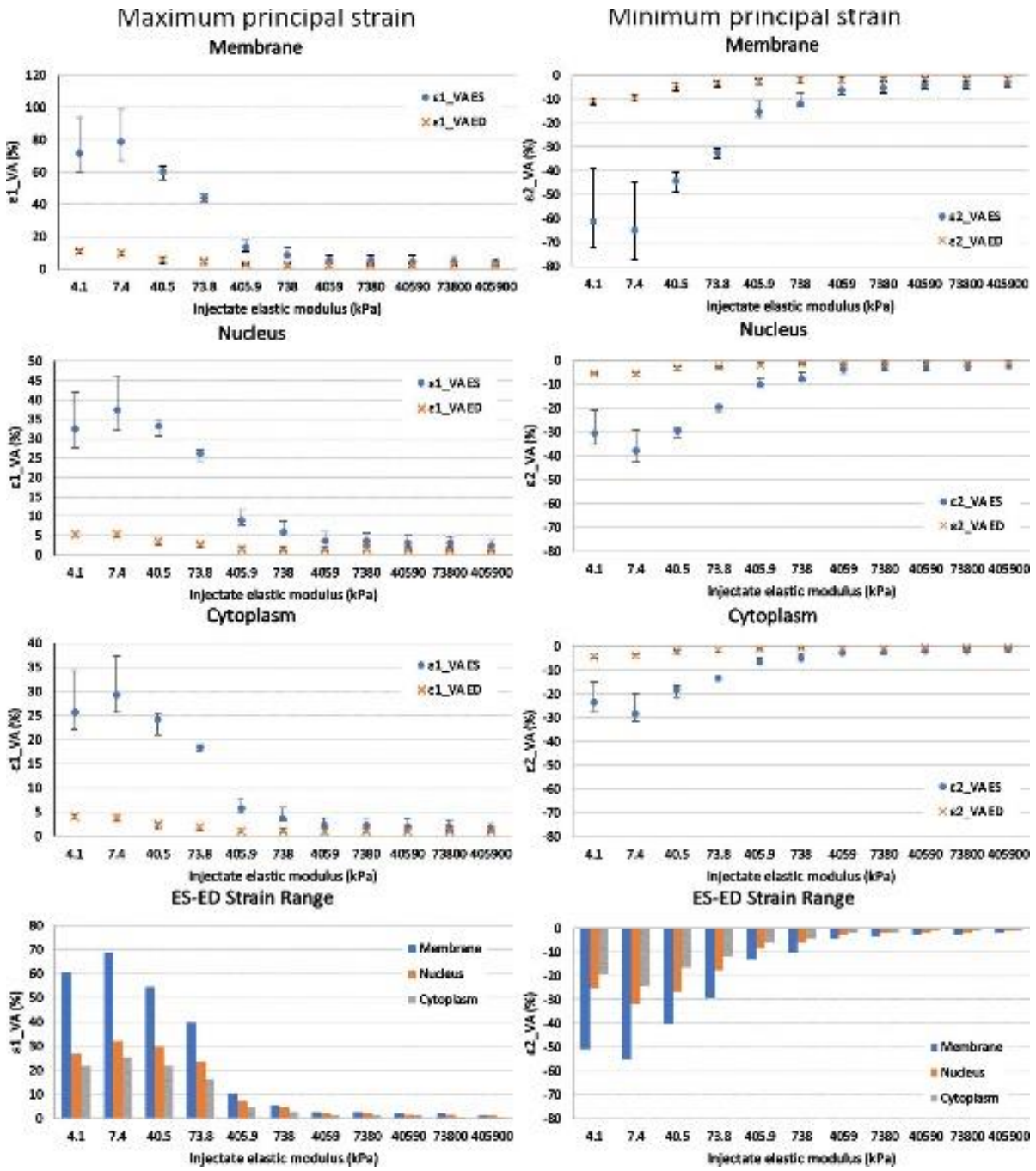

Figure 4. Maximum (a-c) and minimum (d-f) principal strains in the membrane, nucleus, and cytoplasm of transplanted cells at end-systole (ES) and end-diastole (ES) versus injectate elastic modulus. ES-ED range of maximum (g) and minimum (h) principal strain versus injectate elastic modulus for the three cell components. (Data in a to f are median, error bars represent interquartile range).

3.3 Mechanically induced cellular TGF-β expression

An optimised finite element mesh with 7,697, 1,186, and 122,694 elements in the cell body, focal adhesion, and substrate, respectively, was selected following a mesh sensitivity study with a maximum of 15% biaxial strain in the substrate (Figure 5).

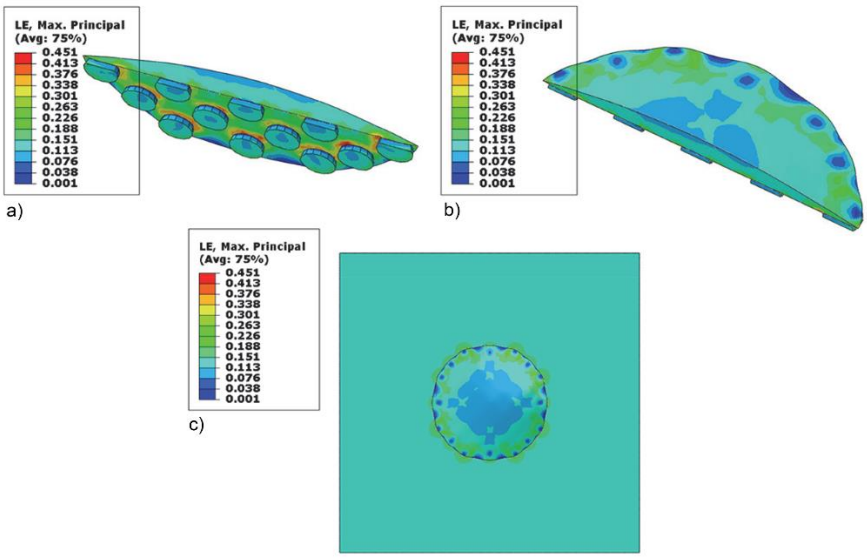

Figure 5. Contour plots of maximum principal strain in the focal adhesions (a), cell body (b), and substrate-cell assembly (c) from substrate biaxial strain of 15% for optimised mesh densities.

The mean volume-averaged maximum principal strain in the cell body and focal adhesions increased linearly with increasing substrate strain ε_{Sub} = 5% to 20% (Figure 6 a). The relationship of the maximum principal strain in the cell with the substrate strain was expressed as a linear function using Eq. (15):

$$\varepsilon_{Cell} = 0.84\,\varepsilon_{Sub} + 0.37, \tag{21}$$

where ε_{Sub} is the substrate strain ranging from 5% to 20%, and ε_{Cell} is the mean volume-averaged maximum principal strain in the cell body and the focal adhesions.

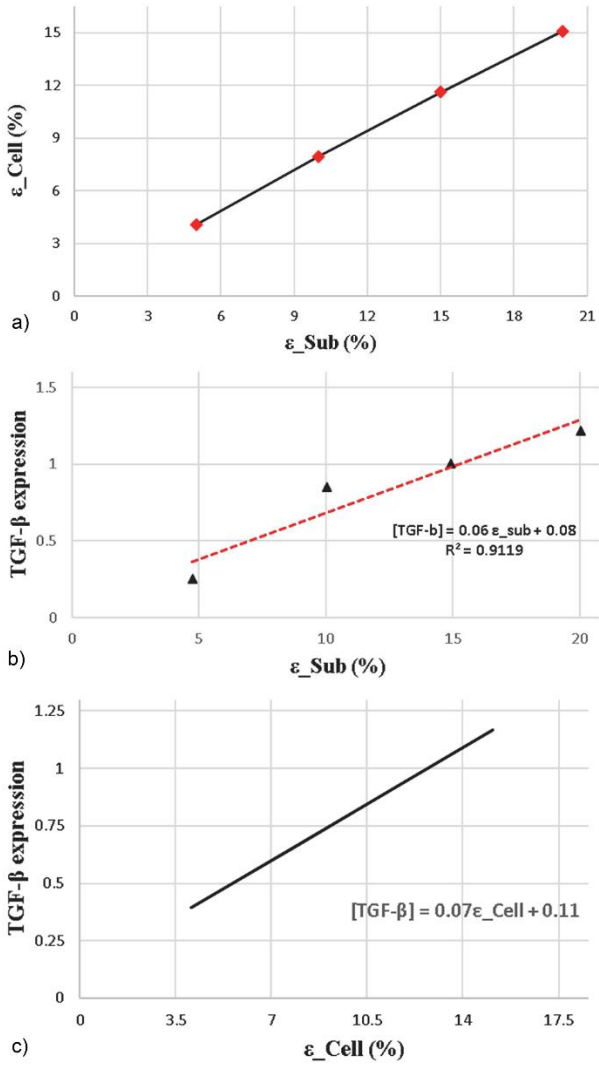

Figure 6. a) Mean volume-averaged maximum principal strain in a single cell stretched on an elastic substrate versus substrate strain. The finite element model computed volume-averaged strain (solid diamonds) is shown with the strain predicted in the cell for increasing substrate strain with Eqn. (21) (solid line). b) TGF-β mRNA expression in a stretched cell on an elastic substrate versus substrate strain showing experimental data of TGF-β mRNA expression from Hirakata et al. (1997) (solid triangles) and a linear fit (dashed line). c) Mechanically induced TGF-β mRNA expression versus mean volume-averaged maximum principal strain in the cell.

A linear fit of the relationship of the cell deformation with TGF-β expression was obtained using the finite element results (Figure 6 a) and the experimental data by Hirakata et al. (1997) (Figure 6 b).

Quantitative data of the TGF-β expression as a function of substrate strain were extracted from Hirakata et al. (1997), Figure 3. Four data pairs were obtained, each corresponding to the substrate strain and the expression of TGF-β (Figure 6 b). Using Eqn. (14), the linear function of TGF-β expression with substrate strain is:

$$\text{TGF-}\beta = 0.06\,\varepsilon_{\text{Sub}} + 0.08\,. \tag{22}$$

The results from the finite element model and the mathematical model were combined using Eq. (16) to describe TGF-β mRNA expression as a function of cell strain:

$$\text{TGF-}\beta = 0.07\,\varepsilon_{\text{Cell}} + 0.11\,, \tag{23}$$

illustrated in Figure 6 (c).

The TGF-β mRNA expression of the cells embedded in the intramyocardial biomaterial injectate decreased with increasing injectate stiffness (Figure 7). The expression of TGF-β in the injected cells was determined using Eqn. (23) and the cell's ES-ED ranges of maximum principal strain (Figure 4 Figure 4g). However, the extrapolation beyond the strain range considered by Hirakata et al. (1997) was required, and it was assumed that the linear relationship is valid in the ES-ED strain range domain.

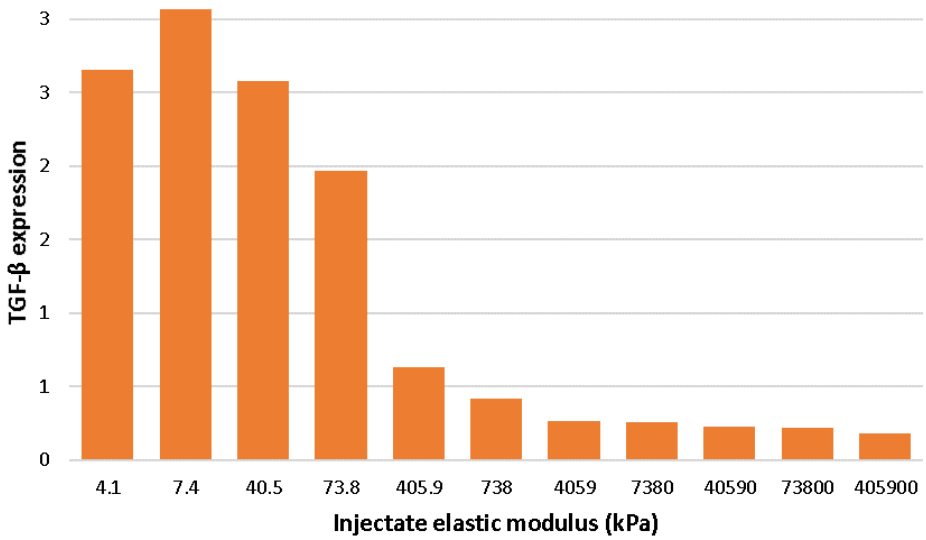

Figure 7. Predicted mechanically induced TGF-β mRNA expression in transplanted cells in the injectate versus injectate elastic modulus.

4. Discussion

Understanding the mechanotransduction involved in cardioprotective paracrine signalling in cell therapies for MI is critical for optimising these therapies. The present computational study demonstrated the effect of the stiffness of the biomaterial injectate on the mechanics and TGF-β expression of cells intramyocardially transplanted with the biomaterial. The variation of the

injectate stiffness can be used to guide deformation and associated biochemical signalling of the transplanted cells in the injectate. Soft injectates promise the most beneficial effects as the cell deformation is more sensitive to a change in injectate stiffness when it is similar to the transplanted cells' stiffness compared to a larger injectate stiffness.

A decrease in strain in the injectate was predicted for an increasing elastic modulus of the injectate. Similar observations were reported by Sirry et al. (2015), where stiffer injectate resulted in less deformation within an acellular injectate region of the sub-model. The current study investigated a wide range of injectate stiffness, with the upper range of the elastic modulus of $E_{inj} > 738$ kPa being unrealistic for PEG hydrogels and other injectable biomaterials (Singelyn et al. 2012; Rizzi et al. 2006). It was shown that the deformations induced in the injectate are negligible from a particular threshold of the injectate elastic modulus.

For the transplanted cells in the injectate, a decrease in ES and ED strains and the associated ES-ED strain range was predicted for increasing injectate stiffness. It was also observed that the cell mechanics was considerably more sensitive to environmental stiffness changes for soft ($E_{inj} \leq 738$ kPa) than stiff injectates ($E_{inj} > 738$ kPa).

Interestingly, an increase in cell strain was observed for an increase in injectate stiffness from $E_{inj} = 4.1$ kPa to 7.4 kPa. This contrasting cell behaviour may reveal a threshold of the injectate stiffness at which the mechanical response of the cells changes. This change may be explained when considering the elastic modulus of the cellular components, namely E = 1.7 kPa for the membrane, 5 kPa for the nucleus and 8 kPa for the cytoplasm. The injectate with $E_{inj} = 4.1$ kPa had a lower elastic modulus than the bulk of the cellular structure (i.e. cytoplasm and nucleus) and transferred less deformation to the cells than the injectate with $E_{inj} = 7.4$ kPa that more closely matches the elastic modulus of cytoplasm and nucleus.

It is well-established that cyclic mechanical loads *in vivo* and *in vitro* induce biochemical responses in cells (Seko et al. 1999; Shradhanjali et al. 2017; Tian et al. 2016; Zheng et al. 2001). Bhang et al. (2010) showed that cyclic mechanical strain promotes the expression of cardiomyogenic markers in bone marrow-derived mesenchymal stem cells and, combined with TGF-β, leads to enhanced expression of cardiac-specific genes.

The developed finite element model based on experimental data from Hirakata et al. (1997) predicted a linear relationship between cell and substrate deformation, similar to the results of Abdalrahman et al. (2017). Data from Hirakata et al. (1997) further showed a linear relationship

between biaxial substrate strain (between 5% and 20%) and cellular TGF-β expression. Implementing this relationship in the substrate-cell stretch finite element model predicted a linear increase in TGF-β expression with increased cell strain. Based on the effect of injectate stiffness on cellular deformation, a higher sensitivity of TGF-β expression to a change in the environmental stiffness was predicted for a low injectate stiffness ($E_{inj} \leq 738$ kPa) compared to a high injectate stiffness ($E_{inj} > 738$ kPa).

The numerical cell seeding algorithm randomly placed cells in the microstructural model's entire volume. Six of the 15 seeded cells were not used for the mechanical analysis due to their location in the tissue domain and vicinity of model boundaries and interfaces. Expanding the seeding algorithm to monitor the location of the cells will provide more control over the seeding process and the number of cells available for analysis. A further extension of the cell seeding can be directed, rather than random, cell placement to determine the impact of cell locations on their mechanics and therapeutic signalling. Such a comprehensive study can help design cell patterns within the injectate at the culture stage and when targeted spatial delivery into the heart becomes available.

The cellular components were treated as isotropic and compressible materials with Neo-Hookean strain energy density functions. The constitutive equations did not consider the active processes involved in the cell (e.g. actin polymerisation and depolymerisation). Including these dynamic cytoskeletal processes will allow for assessing the medium- and long-term structural responses of the transplanted cells.

The data on mechanically-induced growth factor production in the literature are commonly from experiments performed for several hours (Zheng et al. 2001). The kinematics of TGF-β expression was not considered in the current model because the time scale (microseconds) was beyond that of biochemical reactions involved in signalling pathways. A quantitatively accurate model will require information on the entire biochemical pathway of TGF-β in mesenchymal stem cells.

Additional growth factors and other biochemical factors can be included to extend the application of the current work, such as VEGF, known for its role in the neovascularisation of the damaged tissue and responsible for new vessel formation in the infarcted tissue.

The sub-model predicted deformations of therapeutic cells embedded in the injectate beyond the strain range obtained from the experiment by Hirakata et al. (1997). Employing the

developed relationship of the deformation-induced cellular TGF-β expression was based on the assumption that the relationship is valid beyond the experimental strain range (20%). Further investigations or experiments are needed to confirm the validity of the linear increase in TGF-β expression in the ES-ED strain range covered in the cell deformation at the cellular scale.

The effect of the biomaterial injectate on the ventricular function of the infarcted heart has not been considered in the current study. However, functional improvement is essential for optimising biomaterial and stem cell-based therapy for MI and will be included in future work.

5. Conclusions

The current study is the first to quantify the mechanotransduction of therapeutic cells intramyocardially transplanted into the infarcted heart using a biomaterial injectate.

The developed microstructural finite element model of the myocardium and biomaterial injectate at cellular length scale enables quantifying micromechanics and signalling of transplanted cells during a cardiac cycle. The coupling of the microstructural and biventricular cardiac finite element models provides an *in silico* tool to assess and optimise the mechanical support from the biomaterial and the cardioprotective signalling of the transplanted cells in the heart.

The platform offers a broader scope on therapeutic biomaterial and cell injections for MI, e.g. timing of the injection after infarction and cellular expression of other biochemical factors, and for other cardiac conditions such as heart failure.

Data availability

Computational models, custom code, and data supporting this study are available on the University of Cape Town's institutional data repository (ZivaHub) at http://doi.org/10.25375/uct.22673884 as Motchon YD, Sack KL, Sirry MS, Nchejane NJ, Abdalrahman T, Nagawa J, Kruger M, Pauwels E, Van Loo D, De Muynck A, Van Hoorebeke L, Davies NH, Franz T. Data for "In silico mechanics and TGF-ß expression of stem cells intramyocardially transplanted with a biomaterial injectate for treatment of myocardial infarction". ZivaHub, 2023, DOI: 10.25375/uct.22673884.

Funding

This work was financially supported by the National Research Foundation of South Africa (IFR14011761118 to TF), the South African Medical Research Council (SIR328148 to TF), the CSIR Centre for High Performance Computing (CHPC Flagship Project Grant IRMA9543 to TF), and the Dr. Leopold und Carmen Ellinger Stiftung (UCT Three-Way PhD Global Partnership Programme Grant DAD937134 to TF). The funders had no role in study design, data collection and analysis, decision to publish, or preparation of the manuscript. Any opinion, findings, conclusions, and recommendations expressed in this publication are those of the authors, and therefore, the funders do not accept any liability.

Competing Interests

The authors declare that they have no competing interests.

Credit Author Contributions

YDM: Data curation, Formal analysis, Investigation, Methodology, Project administration, Software, Validation, Visualization, Writing – Original Draft Preparation, Writing – Review & Editing

KLS: Methodology, Software, Supervision, Writing – Review & Editing

MSS: Methodology, Software, Supervision, Writing – Review & Editing

NJN: Methodology, Writing – Review & Editing

TA: Methodology, Supervision, Writing – Review & Editing

JN: Methodology, Writing – Review & Editing

MK: Investigation, Writing – Review & Editing

EP: Investigation, Methodology, Writing – Review & Editing

DVL: Investigation, Methodology, Writing – Review & Editing

ADM: Investigation, Writing – Review & Editing

LVH: Resources, Methodology, Supervision, Writing – Review & Editing

NHD: Conceptualization, Data curation, Funding acquisition, Methodology, Project administration, Resources, Supervision, Validation, Writing – Review & Editing

TF: Conceptualization, Data curation, Funding acquisition, Methodology, Project administration, Resources, Supervision, Validation, Writing – Original Draft Preparation, Writing – Review & Editing

References

Abdalrahman T, Dubuis L, Green J, Davies N, Franz T (2017) Cellular mechanosensitivity to substrate stiffness decreases with increasing dissimilarity to cell stiffness. Biomech Model Mechanobiol 16:2063-2075.

Alrefai MT, Murali D, Paul A, Ridwan KM, Connell JM, Shum-Tim D (2015) Cardiac tissue engineering and regeneration using cell-based therapy. Stem cells and cloning: advances and applications 8:81.

Beltrami AP, Barlucchi L, Torella D, Baker M, Limana F, Chimenti S, Kasahara H, Rota M, Musso E, Urbanek K, Leri A, Kajstura J, Nadal-Ginard B, Anversa P (2003) Adult cardiac stem cells are multipotent and support myocardial regeneration. Cell 114:763-776.

Bhang SH, Gwak SJ, Lee TJ, Kim SS, Park HH, Park MH, Lee DH, Lee SH, Kim BS (2010) Cyclic mechanical strain promotes transforming-growth-factor-β1-mediated cardiomyogenic marker expression in bone-marrow-derived mesenchymal stem cells in vitro. Biotechnology and applied biochemistry 55:191-197.

Caille N, Thoumine O, Tardy Y, Meister JJ (2002) Contribution of the nucleus to the mechanical properties of endothelial cells. J Biomech 35:177-187.

Cassino TR, Drowley L, Okada M, Beckman SA, Keller B, Tobita K, Leduc PR, Huard J (2012) Mechanical loading of stem cells for improvement of transplantation outcome

in a model of acute myocardial infarction: The role of loading history. Tissue Eng Part A 18:1101-1108.

Ciuffreda MC, Malpasso G, Chokoza C, Bezuidenhout D, Goetsch KP, Mura M, Pisano F, Davies NH, Gnecchi M (2018) Synthetic extracellular matrix mimic hydrogel improves efficacy of mesenchymal stromal cell therapy for ischemic cardiomyopathy. Acta Biomater 70:71-83.

Di Angelantonio E, Kaptoge S, Pennells L, De Bacquer D, Cooney MT, Kavousi M, Stevens G, Riley L, Savin S, Altay S, Amouyel P, Assmann G, Bell S, Ben-Shlomo Y, Berkman L, Beulens JW, Bjorkelund C, Blaha MJ, Blazer DG, Bolton T, Bonita R, Brenner BH, Brunner EJ, Casiglia E, Chamnan P, Choi YH, Chowdhury R, Coady S, Crespo CJ, Cushman M, Dagenais GR, D'Agostino RB, Daimon M, Davidson KW, Engstrom G, Fang XH, Ford I, Gallacher J, Gansevoort RT, Gaziano TA, Giampaoli S, Grandits G, Grimsgaard S, Grobbee DE, Gudnason V, Guo Q, Humphries S, Iso H, Jukema JW, Kauhanen J, Kengne AP, Khalili D, Khan T, Knuiman M, Koenig W, Kromhout D, Krumholz HM, Lam TH, Laughlin G, Ibanez AM, Moons KGM, Nietert PJ, Nordestgaard BG, O'Donnell C, Palmieri L, Patel A, Perel P, Price JF, Costa RBDE, Ridker PM, Rodriguez B, Rosengren A, Roussel R, Sakurai M, Salomaa V, Sato S, Schottker B, Shara N, Shaw JE, Shin HC, Simons LA, Sofianopoulou E, Sundstrom J, Tolonen H, Ueshima H, Volzke H, Wallace RB, Wareham NJ, Willeit P, Wood D, Wood A, Zhao D, Onuma O, Woodward M, Danaei G, Roth G, Mendis S, Graham I, Varghese C, Ezzati M, Jackson R, Danesh J, Di Angelantonio E, Nambi V, Matsushita K, Couper D, Diabetes A, Zimmet PZ, Barr ELM, Atkins R, Whincup PH, Study B, Kiechl S, Willeit J, Rungger G, Sofat R, Dale C, Casas JP, Ben-Shlomo Y, Tikhonoff V, Casiglia E, Hunt KJ, Sutherland SE, Nietert PJ, Psaty BM, Tracy R, Frikke-Schmidt

R, Jensen GB, Schnohr P, Palmieri L, Donfrancesco C, Vanuzzo D, Panico S, Giampaoli S, Balkau B, Bonnet F, Fumeron F, Simons J, McLachlan S, Guralnik J, Khaw KT, Brenner H, Zhang Y, Holleczek B, Cohort F, Salomaa V, Vartiainen E, Jousilahti P, Harald K, Massaro JJ, Pencina M, Ramachandran V, Susa S, Oizumi T, Kayama T, Rosengren A, Wilhelmsen L, Lissner L, Hange D, Mehlig K, Hata J, Yoshida D, Hirakawa Y, Rodriguez B, Rutters F, Elders PJM, Kyowa I, Kiyama M, Yamagishi K, Iso H, Tuomainen TP, Virtanen J, Salonen JT, Meade TW, Nilsson PM, Melander O, de Boer IH, DeFilippis AP, Kuller LH, Juan SI, Gillum RF, Humphries S, Kirkland S, Shimbo D, Schwartz JE, Kiyama M, Imano H, Iso H, van der Harst P, Hillige JL, Bakker SJ, Crespo CJ, Dallongeville J, Ferrieres J, Moitry M, Stott DJ, Despres JP, Laughlin GA, Daniels LB, McEvoy LK, Aspelund T, Thorsson B, Gudmundsson EF, Aribas E, Rueda-Ochoa OL, Ikram MK, Heshmatollah A, Ikram MA, Woodward M, Dorr M, Nauck M, Howard B, Zhang Y, Ben-Shlomo Y, Can G, Ishizaki M, Wilsgaard T, Mathiesen E, Giedraitis V, Ingelsson M, Cook N, Buring J, van der Schouw YT, Claessen H, Rothenbacher D, Arndt V, Study WI, Shipley M, Buring J, Packard C, Robertson M, Young R, Feskens E, Geleijnse JM, Fang X, Gu DF, Huxley R, Imai Y, Kim HC, Lam TH, Pan WH, Rodgers A, Suh I, Ueshima H, Woodward M, Town A, Okayama A, Ueshima H, Maegawa H, Nakamura M, Aoki N, Wu ZS, Yao CH, Wu ZS, Luszcz M, Tang Z, Liu LS, Xie JX, Norton R, Ameratunga S, MacMahon S, Whitlock G, Knuiman MW, Christensen H, Wu XG, Zhou J, Yu XH, Tamakoshi WA, Pan WH, Wu ZL, Chen LQ, Shan GL, Sritara P, Gu DF, Duan XF, MacMahon S, Norton R, Whitlock G, Jackson R, Li YH, Lam TH, Jiang CQ, Ninomiya T, Hata J, Hirakawa Y, Woo J, Ho SC, Hong Z, Huang MS, Zhou B, Fuh JL, Ueshima H, Kita Y, Choudhury SR, Suh I, Jee SH, Kim IS, Giles GG, Hashimoto T, Sakata K,

Dobson A, Imai Y, Ohkubo T, Hozawa A, Jamrozik K, Knuiman MW, Hobbs M, Broadhurst R, Nakachi K, Fang XH, Li SC, Yang QD, Chen ZM, Tanaka SH, Town S, Kita Y, Ueshima H, Horibe H, Matsutani Y, Kagaya M, Hughes K, Lee J, Heng D, Chew SK, Zhou BF, Zhang HY, Shimamoto K, Saitoh S, Li ZZ, Zhang HY, Saitoh S, Li ZZ, Zhang HY, Norman P, Jamrozik K, He Y, Lam TH, Yao SX, Wang M, Liu J, Zhang XG, Mahavanakul W, Wettana B, Boonkert P, Poppe K, Azizi F, Zadehvakili A, Hadaegh F, Grp WCRCW (2019) World Health Organization cardiovascular disease risk charts: Revised models to estimate risk in 21 global regions. Lancet Glob Health 7:E1332-E1345.

Duran JM, Makarewich CA, Sharp TE, Starosta T, Zhu F, Hoffman NE, Chiba Y, Madesh M, Berretta RM, Kubo H (2013) Bone-derived stem cells repair the heart after myocardial infarction through transdifferentiation and paracrine signaling mechanisms. Circulation research 113:539-552.

Finegold JA, Asaria P, Francis DP (2013) Mortality from ischaemic heart disease by country, region, and age: Statistics from World Health Organisation and United Nations. Int J Cardiol 168:934-945.

Galie P, Russell M, Westfall M, Stegemann J (2012) Interstitial fluid flow and cyclic strain differentially regulate cardiac fibroblast activation via AT1R and TGF-β1. Experimental cell research 318:75-84.

Gao LR, Chen Y, Zhang NK, Yang XL, Liu HL, Wang ZG, Yan XY, Wang Y, Zhu ZM, Li TC (2015) Intracoronary infusion of Wharton's jelly-derived mesenchymal stem cells in acute myocardial infarction: Double-blind, randomized controlled trial. BMC medicine 13:162.

Gnecchi M, Zhang Z, Ni A, Dzau VJ (2008) Paracrine mechanisms in adult stem cell signaling and therapy. Circ Res 103:1204-1219.

Guccione J, McCulloch A (1993) Mechanics of active contraction in cardiac muscle: Part i—constitutive relations for fiber stress that describe deactivation. Journal of Biomechanical Engineering 115:72-81.

Guccione J, Waldman L, McCulloch A (1993) Mechanics of active contraction in cardiac muscle: Part II—cylindrical models of the systolic left ventricle. Journal of Biomechanical Engineering 115:82-90.

Guo HD, Wang HJ, Tan YZ, Wu JH (2011) Transplantation of marrow-derived cardiac stem cells carried in fibrin improves cardiac function after myocardial infarction. Tissue Eng Part A 17:45-58.

Hirakata M, Kaname S, Chung UG, Joki N, Hori Y, Noda M, Takuwa Y, Okazaki T, Fujita T, Katoh T, Kurokawa K (1997) Tyrosine kinase dependent expression of TGF-beta induced by stretch in mesangial cells. Kidney Int 51:1028-1036.

Holmes JW, Borg TK, Covell JW (2005) Structure and mechanics of healing myocardial infarcts. Annu Rev Biomed Eng 7:223-253.

Holmes JW, Nunez JA, Covell JW (1997) Functional implications of myocardial scar structure. Am J Physiol 272:H2123-2130.

Holzapfel GA, Ogden RW (2009) Constitutive modelling of passive myocardium: A structurally based framework for material characterization. Philos Trans A Math Phys Eng Sci 367:3445-3475.

Hood WB, Bianco JA, Kumar R, Whiting RB (1970) Experimental myocardial infarction: IV. Reduction of left ventricular compliance in the healing phase. The Journal of Clinical Investigation 49:1316-1323.

Kocher AA, Schuster MD, Szabolcs MJ, Takuma S, Burkhoff D, Wang J, Homma S, Edwards NM, Itescu S (2001) Neovascularization of ischemic myocardium by human bone-marrow-derived angioblasts prevents cardiomyocyte apoptosis, reduces remodeling and improves cardiac function. Nat Med 7:430-436.

Masschaele BC, Cnudde V, Dierick M, Jacobs P, Van Hoorebeke L, Vlassenbroeck J (2007) UGCT: New x-ray radiography and tomography facility. Nuclear Instruments and Methods in Physics Research Section A: Accelerators, Spectrometers, Detectors and Associated Equipment 580:266-269.

Mendis S, Puska P, Norrving B (2011) Global atlas on cardiovascular disease prevention and control. World Health Organization,

Mininni S, Diricatti G, Vono MC, Giglioli C, Margheri M, Olivo G, Gensini G, Galanti G (1996) Noninvasive evaluation of right ventricle systolic pressure during dynamic exercise by saline-enhanced doppler echocardiography in progressive systemic sclerosis. Angiology 47:467-474.

Motchon YD, Sack KL, Sirry MS, Kruger M, Pauwels E, Van Loo D, De Muynck A, Van Hoorebeke L, Davies NH, Franz T (2023) Effect of biomaterial stiffness on cardiac mechanics in a biventricular infarcted rat heart model with microstructural representation of in situ intramyocardial injectate. Int J Numer Meth Bio -:e3693.

Nguyen PK, Rhee JW, Wu JC (2016) Adult stem cell therapy and heart failure, 2000 to 2016: A systematic review. JAMA Cardiol 1:831-841.

Opie LH, Mayosi BM (2005) Cardiovascular disease in sub-Saharan Africa. Circulation 112:3536-3540.

Pacher P, Mabley JG, Liaudet L, Evgenov OV, Marton A, Hasko G, Kollai M, Szabo C (2004) Left ventricular pressure-volume relationship in a rat model of advanced aging-associated heart failure. Am J Physiol Heart Circ Physiol 287:H2132-2137.

Rashid FN, Clayton ZE, Ogawa M, Perdomo J, Hume RD, Kizana E, Chong JJH (2021) Platelet derived growth factor-A (Pdgf-a) gene transfer modulates scar composition and improves left ventricular function after myocardial infarction. Int J Cardiol 341:24-30.

Reichek N, Devereux RB (1982) Reliable estimation of peak left ventricular systolic pressure by M-mode echographic-determined end-diastolic relative wall thickness: Identification of severe valvular aortic stenosis in adult patients. Am Heart J 103:202-203.

Rizzi SC, Ehrbar M, Halstenberg S, Raeber GP, Schmoekel HG, Hagenmüller H, Müller R, Weber FE, Hubbell JA (2006) Recombinant protein-co-PEG networks as cell-adhesive and proteolytically degradable hydrogel matrixes. Part II: Biofunctional characteristics. Biomacromolecules 7:3019-3029.

Robinton DA, Daley GQ (2012) The promise of induced pluripotent stem cells in research and therapy. Nature 481:295-305.

Sack KL, Aliotta E, Ennis DB, Choy JS, Kassab GS, Guccione JM, Franz T (2018) Construction and validation of subject-specific biventricular finite-element models of healthy and failing swine hearts from high-resolution DT-MRI. Front Physiol 9:539.

Saeed M, Sharabani-Yosef O, Weihs D, Gefen A (2016) A phase-contrast microscopy-based method for modeling the mechanical behavior of mesenchymal stem cells. Comput Methods Biomech Biomed Engin 19:1359-1362.

Seko Y, Seko Y, Takahashi N, Shibuya M, Yazaki Y (1999) Pulsatile stretch stimulates vascular endothelial growth factor (VEGF) secretion by cultured rat cardiac myocytes. Biochem Biophys Res Commun 254:462-465.

Shradhanjali A, Riehl BD, Lee JS, Ha L, Lim JY (2017) Enhanced cardiomyogenic induction of mouse pluripotent cells by cyclic mechanical stretch. Biochem Biophys Res Commun 488:590-595.

Shudo Y, Miyagawa S, Ohkura H, Fukushima S, Saito A, Shiozaki M, Kawaguchi N, Matsuura N, Shimizu T, Okano T (2013) Addition of mesenchymal stem cells enhances the therapeutic effects of skeletal myoblast cell-sheet transplantation in a rat ischemic cardiomyopathy model. Tissue Engineering Part A 20:728-739.

Singelyn JM, Sundaramurthy P, Johnson TD, Schup-Magoffin PJ, Hu DP, Faulk DM, Wang J, Mayle KM, Bartels K, Salvatore M, Kinsey AM, Demaria AN, Dib N, Christman KL (2012) Catheter-deliverable hydrogel derived from decellularized ventricular extracellular matrix increases endogenous cardiomyocytes and preserves cardiac function post-myocardial infarction. J Am Coll Cardiol 59:751-763.

Sirry MS, Davies NH, Kadner K, Dubuis L, Saleh MG, Meintjes EM, Spottiswoode BS, Zilla P, Franz T (2015) Micro-structurally detailed model of a therapeutic hydrogel injectate in a rat biventricular cardiac geometry for computational simulations. Comput Methods Biomech Biomed Engin 18:325-331.

Strauer BE, Steinhoff G (2011) 10 years of intracoronary and intramyocardial bone marrow stem cell therapy of the heart: From the methodological origin to clinical practice. J Am Coll Cardiol 58:1095-1104.

Tian Y, Gawlak G, O'Donnell JJ, 3rd, Birukova AA, Birukov KG (2016) Activation of vascular endothelial growth factor (VEGF) receptor 2 mediates endothelial permeability caused by cyclic stretch. J Biol Chem 291:10032-10045.

Tomita S, Li RK, Weisel RD, Mickle DA, Kim EJ, Sakai T, Jia ZQ (1999) Autologous transplantation of bone marrow cells improves damaged heart function. Circulation 100:II247-256.

Tyberg JV, Forrester JS, Wyatt HL, Goldner SJ, Parmley WW, Swan HJ (1974) An analysis of segmental ischemic dysfunction utilizing the pressure-length loop. Circulation 49:748-754.

Villarreal FJ, Lew WY, Waldman LK, Covell JW (1991) Transmural myocardial deformation in the ischemic canine left ventricle. Circ Res 68:368-381.

Walker JC, Ratcliffe MB, Zhang P, Wallace AW, Fata B, Hsu EW, Saloner D, Guccione JM (2005) MRI-based finite-element analysis of left ventricular aneurysm. Am J Physiol Heart Circ Physiol 289:H692-700.

Wang W, Tan B, Chen J, Bao R, Zhang X, Liang S, Shang Y, Liang W, Cui Y, Fan G, Jia H, Liu W (2018) An injectable conductive hydrogel encapsulating plasmid DNA-eNOs and ADSCs for treating myocardial infarction. Biomaterials 160:69-81.

Ye L, Zimmermann W-H, Garry DJ, Zhang J (2013) Patching the heart: Cardiac repair from within and outside. Circulation Research 113:922-932.

Zhao L, Liu X, Zhang Y, Liang X, Ding Y, Xu Y, Fang Z, Zhang F (2016) Enhanced cell survival and paracrine effects of mesenchymal stem cells overexpressing hepatocyte growth factor promote cardioprotection in myocardial infarction. Exp Cell Res 344:30-39.

Zheng W, Seftor EA, Meininger CJ, Hendrix MJ, Tomanek RJ (2001) Mechanisms of coronary angiogenesis in response to stretch: Role of VEGF and TGF-beta. Am J Physiol Heart Circ Physiol 280:H909-917.